Effect of pre-strain on springback behavior after air bending in AA 6016-T4: Influence of dislocation density and backstress on prediction accuracy

[1]Md Zahidul Sarkar, [2]Dane Sargeant, [2]Rishabh Sharma, [1]Marko Knezevic,
[3]David T. Fullwood, [2*]Michael P. Miles

[1]Department of Mechanical Engineering, University of New Hampshire, Durham, NH 03824
[2]Department of Manufacturing Engineering, Brigham Young University, Provo, UT 84602
[3]Department of Mechanical Engineering, Brigham Young University, Provo, UT 84602

Abstract

Predicting springback in sheets of aluminum alloys is challenging, especially when a complex strain path is used to form the material. This paper presents results from air bending experiments on AA 6016-T4 sheet material, where pre-strains were first applied to the sheet specimens in uniaxial tension, plane-strain tension, and biaxial tension, at effective strain levels of 6%, 15% and ~20%. The pre-strained specimens were then subjected to air bending in a v-die, using target angles of 100˚, 85˚, and 70˚, after which springback was measured. It was found that greater levels of pre-strain result in larger springback magnitudes, and that the biaxial pre-strained specimens generally exhibited greater springback than the other pre-strained specimens. A CPFE – EPSC model with phenomenological backstress component in the hardening law was used to predict springback magnitude across the different pre-strain paths, pre-strain levels, and imposed air bend angles. It was found that the more significant the strain path change, as from biaxial tension pre-strain followed by bending, the greater the statistically stored dislocation (SSD) development on both the tensile surface of the sheet, and also through the thickness. As such, the influence of backstress on model accuracy was correlated with greater SSD development during bending, where different slip systems were active for each type of pre-strain, thus influencing hardening behavior during the subsequent bending step. By contrast, when the strain path change was less abrupt, as in plane-strain pre-strain followed by bending, SSD development was not as great and the effect of backstress on model accuracy was muted. The use of a phenomenological backstress law, within a CPFE-EPSC framework, is seen to be an accurate and efficient approach to improving springback prediction in Al alloys, especially for strain path changes that can occur during stamping of an industrial part.

Keywords: aluminum alloys; air bending; backstress; springback; strain path change; CPFE-EPSC modeling

1 INTRODUCTION

Prediction of springback in aluminum alloys used for automotive stamped parts is complicated by internal backstress development that occurs during the forming process (Boers et al., 2010). Complex part shapes can require a varying strain path as the material is progressively formed in the dies, making it necessary to characterize both hardening and internal stress behavior using macro and micro approaches. The heat-treatable 6xxx aluminum alloys being employed for automotive lightweighting applications have precipitates that act as barriers to dislocation motion, leading to various dislocation substructures (El-Madhoun et al., 2003). Geometrically necessary dislocations (GNDs) that form during plastic deformation (Ashby, 1970) accumulate in pileups at precipitates and grain boundaries (Shen et al., 1988), or in substructures within grains (Field et al., 2005). Backstresses build up in the strain gradient regions, through interaction between dislocations of the same polarity, and contribute to hardening behavior of the alloy by opposing the applied resolved shear stress necessary for dislocation slip. Upon load reversal, backstresses assist dislocation slip, causing nonlinear unloading and softening and/or lower subsequent yield stresses.

Backstress levels estimated in a recent study were shown to have a significant effect on the elasto-plastic transition and plastic response under strain path changes from biaxial and plane-strain tension to uniaxial tension deformation (Sharma et al., 2022). Another study that included cyclic deformation cycles and various pre-strain conditions in a 7xxx series aluminum showed a decrease in elastic modulus upon unloading-reloading, and an increase in springback with greater pre-strain levels (Yue et al., 2018prin). The importance of including inelastic recovery in the prediction of springback in dual-phase (DP) steel has been seen for sheets first pre-strained in uniaxial tension, then formed into an S-rail shape (Chongthairungruang et al., 2012). A

phenomenological approach where a dynamic modulus using a kinematic hardening law was shown to improve simulated springback predictions (Wagoner et al., 2013).

The aforementioned models may predict deformation response and springback during and after forming, but they are not adequate to simulate the effects of strain path changes on a nonlinear unloading response if backstress evolution is not modeled in the hardening law. In prior work, Yue et al. (Yue et al., 2018) reported a springback prediction error of approximately 17.5% for an 11% uniaxial pre-strain. Liao et al. (Liao et al., 2020) performed twist springback simulations after applying uniaxial pre-strain and found that their simulations had errors of 15% and 12% in the rolling (RD) and transverse (TD) directions. In a similar study performed by Chen et al. (Chen et al., 2021), errors of 28.6% and 14.6% along the RD and the TD directions were observed due to an over-estimation of elastic modulus values in the model. In the case of bending, the plastic anisotropy of the material, as well as the accuracy of the yield function under plane-strain conditions, is considered to be critical to accurate springback prediction (Uemori et al., 2017).

The current work employs a crystal plasticity finite element (CPFE) approach to model various pre-strains followed by pure bending in AA 6016-T4 sheets. An EPSC model within the CPFE framework employs a strain path sensitive dislocation density-based hardening law, and a phenomenological backstress relationship, to predict springback in AA6016-T4 sheet material after the bending step. It builds upon a prior EPSC model that has predicted the microstructural and mechanical response to strain path changes, including non-linear unloading, residual stress fields, the Bauschinger effect, hardening rates, and texture of the material (Zecevic and Knezevic, 2019). Additional prior work that has influenced the current approach includes an EVPSC-FE model that successfully predicted the effect of pre-strain on springback after bending in EDDQ steel sheet (Joo et al., 2023); an EPSC model for predicting reverse and simple loading

deformation in AA6022-T4 (Barrett and Knezevic, 2019); and a modeling study on multi-strain path deformation in AA6016-T4 (Sharma et al., 2022).

2 EXPERIMENTAL METHODS

The springback behavior of AA6016-T4 sheet material was quantified using a 100-ton AccurPress press-brake, where specimens were formed to various bend angles, including 70˚, 85˚, and 100˚ using the same v-die configuration for each angle. As the punch did not compress the sheet fully against the lower V-die shown in Figure 1, various air bending angles (100˚, 85˚, 70˚) were achieved. This is a contrast to bottom bending, where the sheet is fully compressed into the V-die and where only one angle could be obtained, corresponding to the shape of the V-die itself. Three replications were averaged for each pre-strain level and path, as well as each bend angle, to obtain a springback angle.

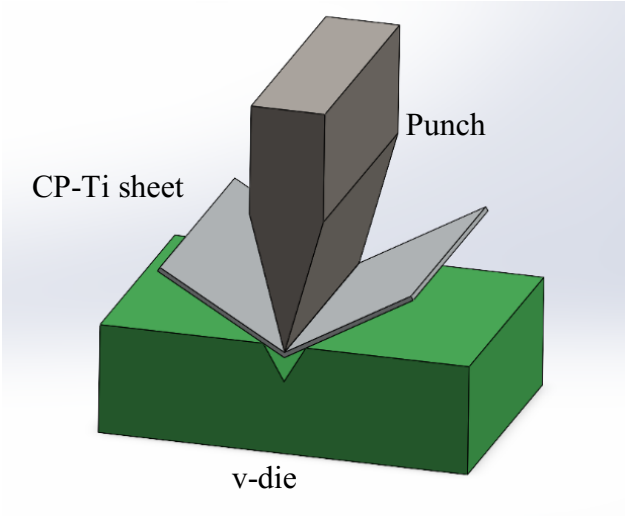

Fig. 1. Tooling configuration for air bending experiments. The punch tip had a radius of 0.8mm and the included v-die angle was 30˚. Different bend angles were achieved by varying the stroke of the punch, which was always short of compressing the material fully into the v-die. Three replications were averaged to obtain a springback angle for each case.

The subsequent springback was analyzed optically using 3-D profile tracing software on a Keyence Digital Microscope, where the sheet profiles at the bottom of the punch stroke, and after unloading,

were compared to evaluate the degree of springback in each case (see Figure 2). Large sheet blanks were first pre-strained to various levels of effective strain (6%, 15%, 20%) in uniaxial tension, plane-strain tension, and biaxial tension. Then smaller 63.5m x 63.5mm specimens were cut from the pre-strained sheets via waterjet. All pre-strained specimens were oriented such that the RD

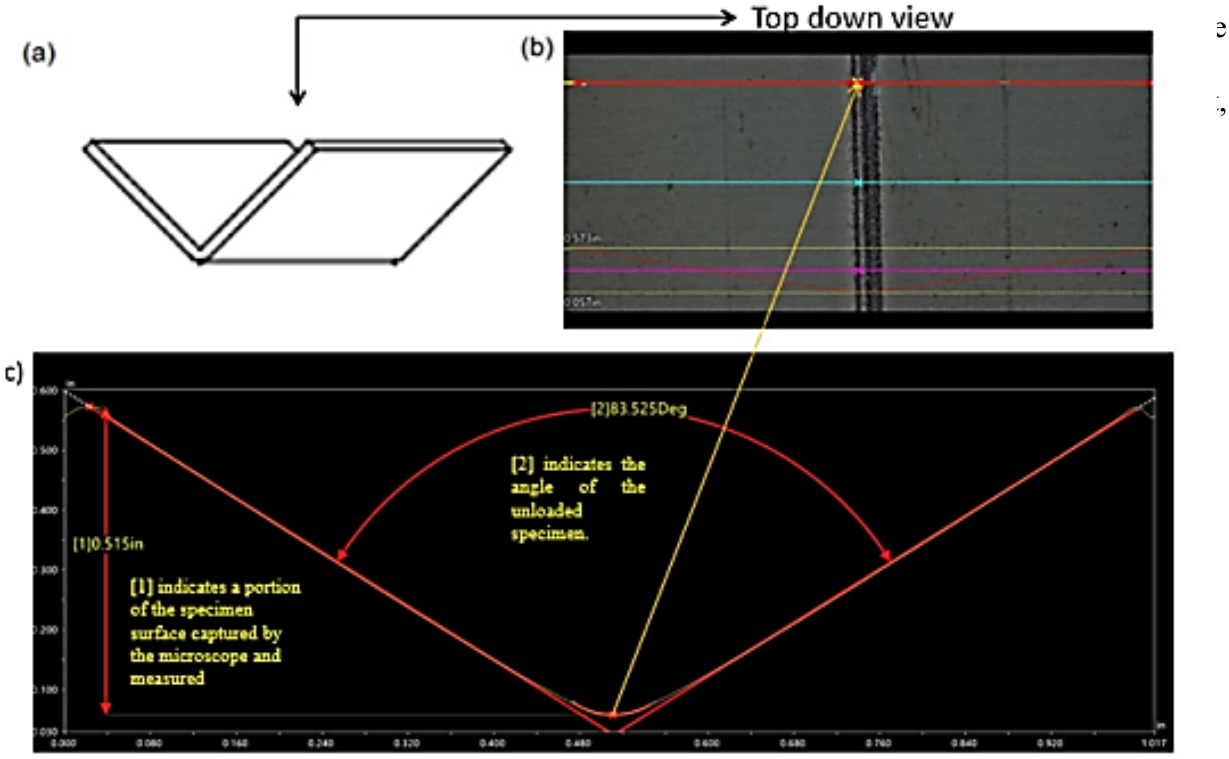

Fig. 2. Springback measurements were performed using a Keyence microscope. (a) After bending each specimen to the desired angle in the v-die, the specimen was removed and the final shape was measured using three scans, as shown in (b). The angle was computed for each scan (c), and the three measurements were averaged.

2.1 Pre-Straining Methods: Biaxial Tension, Plane Strain Tension, and Uniaxial Tension

The biaxial and plane-strain tension tests were guided by a previous study on DP 600 steel sheets by Cheng et. al (Cheng et al., 2017). Forming limits for biaxial tension and plane-strain tension (with the major strain axis oriented along the RD) were measured using an Interlaken hydraulic press with standard Marciniak tooling. The tooling incorporates a 100mm diameter punch with a flat top, making specimen extraction from the pre-strained material convenient for further testing.

Deformation with Marciniak tooling includes the use of a carrier blank that limits the strain localization along the rim of the punch, so that a maximum strain level can be produced across the punch face. All experiments were performed with a clamp load of 200kN, using 0.5mm thick Teflon sheets positioned between the sheet and punch, and mineral oil applied on the punch, Teflon sheet, carrier blank, and sheet specimen. While biaxial specimens were fully clamped, plane-strain tension required some experimentation to find the appropriate specimen width that imposed a plane-strain deformation path. The surface strains on each specimen were measured using Aramis digital image correlation (DIC) equipment attached to the press. The Marcinak tooling and an example of a biaxial pre-strained specimen are shown in Figure 3. Note that for the uniaxial pre-strains, a large tensile specimen was employed, with dimensions of 64mm x 635mm. Following pre-straining, to effective strain levels of 6%, 15%, and 18-20% effective strain, bend specimens were removed from the center of each pre-strained sheet using a shear. The specimens were then subjected to bending experiments, with the tooling shown in Figure 1, using bend angles of 70˚, 85˚, and 100˚ (measured as an included angle).

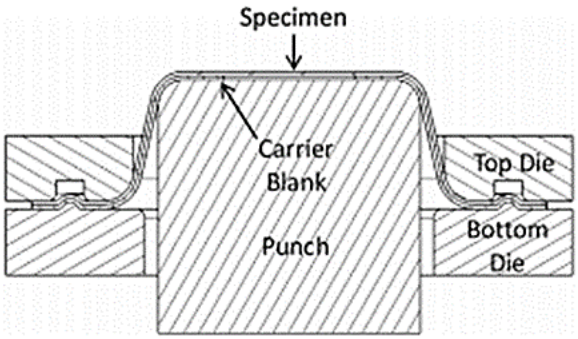

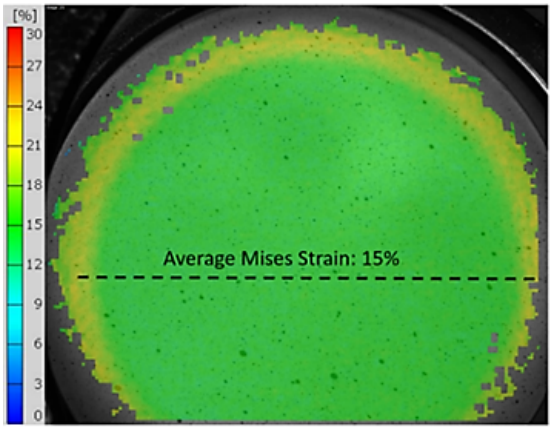

(a) (b)

Fig. 3. (a) Marciniak tooling for biaxial and plane-strain tension pre-strain experiments, and (b) DIC strain map for a 15% pre-strained biaxial-tension specimen. Coupons for bend testing with 63.5mm x 63.5mm dimensions were cut from the center of the flat portion of the Marcinak specimen, after applying different levels of pre-strain.

2.2 Material Characterization

The composition of the 1 mm thick AA6016-T4 alloy sheets used for the experimental work is shown in Table 1. Stress-strain curves produced by uniaxial tension tests provided material properties necessary for initial characterization. Specimens were cut from the sheet along the rolling direction (RD), transverse direction (TD), and 45° to the RD of the sheet according to the ASTM E8 specification. The specimens were pulled at a 1.5 mm/min crosshead displacement rate and the force-strain data were recorded using load cell and extensometer output. Table 2 shows minor differences in the deformation response for the three orientations. The failure strain measured for each orientation ranged from 0.245 to 0.270, with RD exhibiting the greatest.

Table 1. Nominal chemical composition of AA6016-T4.

Al	Si	Mg	Fe	Mn	Zn	Cu	Ti	Cr
96.4-98.8	1.0-1.5	0.25-0.6	0-0.5	0-0.2	0-0.2	0-0.2	0-0.15	0-0.1

Table 2. Tensile properties of AA6016-T4.

Orientation	Young's modulus (GPa)	True failure strain	Yield strength (MPa)	Ultimate tensile strength (MPa)
RD	70.5	0.270	142	344
45˚ to RD	70.8	0.245	140	321
TD	71.7	0.249	140	326

The unstrained base material texture was measured using EBSD to calibrate the model for the AA 6016-T4 alloy. A small sample sectioned from the gauge length of the pre-strained specimens was prepared for microstructure analysis. The microscopy samples were removed using a diamond

blade cutter, to avoid deformation of the material, and mounted in epoxy resin to be polished for EBSD scanning. The ND surface of the samples was first ground with grits of 400, 600, 800, 1200, and 1200 fine abrasive paper. The ground samples were then electropolished using an electrolyte solution of 1:9 ratio of perchloric acid and methanol under 20 volts and 2 amps at room temperature for 30s. The polished samples were milled in an inert argon gas environment by a JEOL ion-beam cross-section polisher to remove the initial strain layer induced by polishing. The surface was first coarsely milled at 5kV and 4.2 atm for 20 mins. A second finer step removed unevenness by milling the surface at 4kV and 6.2 atm for 5 mins. The texture data generated by EBSD for the EPSC model contained approximately 1000 grains that were subsequently compacted to 100 grains for each orientation (Barrett et al., 2019; Eghtesad et al., 2018; Knezevic and Landry, 2015). The compaction is done to decrease computation time. Figure 4 shows the original and the compacted pole figures for the unstrained base material.

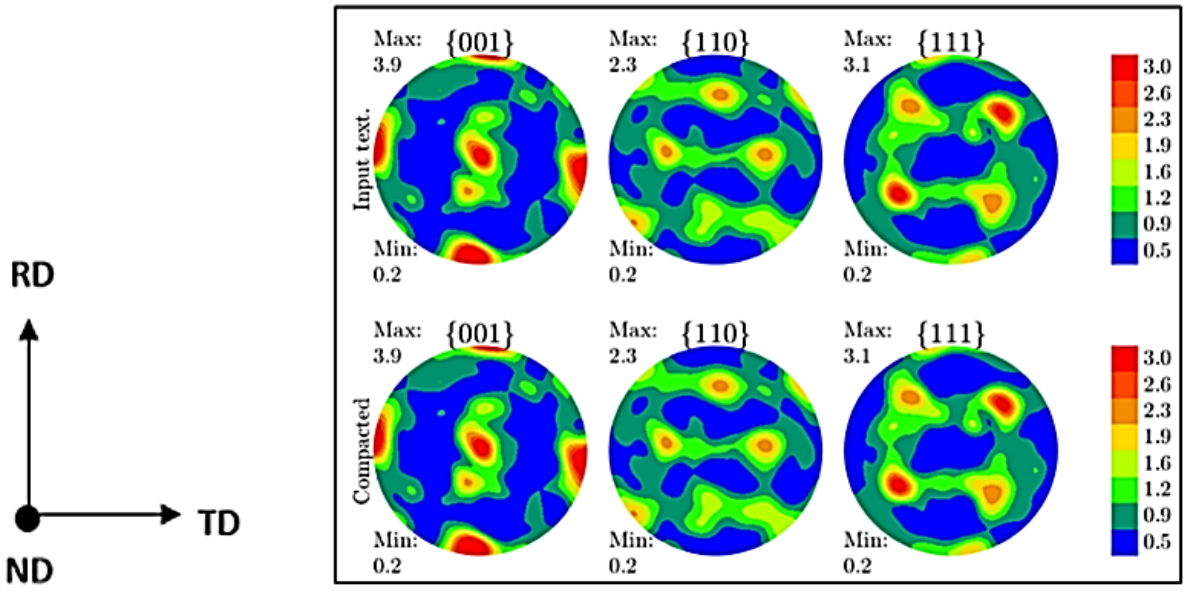

Fig. 4. Original texture for AA6016-T4 comprising ~1000 grains (top), and texture data compacted to 100 grains (bottom) for EPSC simulations.

As discussed in prior work by the authors, GND density measurement by high resolution electron backscatter diffraction (HREBSD) for the unstrained AA 6061-T4 material was also performed to confirm that the dislocation density estimate for the initial state of the material was reasonable for the EPSC model (Sharma et al., 2022). The rationale for this is discussed further below.

3 MODEL DESCRIPTION

Simulations of pre-straining, air bending, and springback were performed using the CPFE-EPSC framework. The model was originally developed by Zecevic and Knezevic (Zecevic and Knezevic, 2019) and since the development has been used to predict plastic deformation under different strain paths and including cyclic loading in prior works involving AA 6016-T4 (Daroju et al., 2022; Sharma et al., 2022). In the description that follows, the subscript FE indicates variables returned/passed from/to the Abaqus FEM solver to the UMAT subroutine. Every integration/material point of the FE mesh embeds a set of weighted crystal orientations representing texture of the polycrystalline AA 6016 aggregate. The CPFE-EPSC material model returns Cauchy stress at the end of each strain increment, $\boldsymbol{\sigma}_{FE}^{t+\Delta t}$, for an interrogating strain increment, $\Delta\boldsymbol{\varepsilon}_{FE}$, provided by Abaqus. The strain increment is determined based on the boundary conditions applied to the mesh. The strain accommodated by CPFE-EPSC at each integration point is updated according to:

$$\boldsymbol{\varepsilon}_{FE}^{t+\Delta t} = \boldsymbol{\varepsilon}_{FE}^{t} + \Delta\boldsymbol{\varepsilon}_{FE}. \quad (2)$$

In addition to Cauchy stress, the implicit coupling of the EPSC model and FEM requires a Jacobian matrix, $\frac{\partial \Delta \boldsymbol{\sigma}_{FE}}{\partial \Delta \boldsymbol{\varepsilon}_{FE}}$, to be returned for calculating trial displacement fields in arriving at the solution. The Jacobian is (Zecevic and Knezevic, 2019):

$$\frac{\partial \Delta \boldsymbol{\sigma}_{FE}}{\partial \Delta \boldsymbol{\varepsilon}_{FE}} = \frac{\partial \left(\boldsymbol{\sigma}_{FE}^{t+\Delta t} - \boldsymbol{\sigma}_{FE}^{t}\right)}{\partial \Delta \boldsymbol{\varepsilon}_{FE}} = \frac{\partial \Delta \bar{\boldsymbol{\sigma}}}{\partial \Delta \bar{\boldsymbol{\varepsilon}}} = \frac{\partial \left(\bar{\mathbf{L}}^{inc} \Delta \bar{\boldsymbol{\varepsilon}}\right)}{\partial \Delta \bar{\boldsymbol{\varepsilon}}} = \bar{\mathbf{L}}^{inc}, \tag{3}$$

where $\bar{\mathbf{L}}^{inc}$ is the stiffness driven by the Cauchy stress and strain increments (Zecevic and Knezevic, 2019). Other relevant details of the CPFE-EPSC model, including the strain path sensitive hardening law, are found in the appendix. The backstress component of hardening is based on a phenomenological formulation. In particular, it influences unloading, the Bauschinger effect, and hardening. The evolution of backstress on every slip system, τ_{bs}^{s}, is a function of shearing strains on slip systems, $\gamma^{s'}$. The laws for $d\gamma^{s^+} > 0$ and $\tau_{bs}^{s^+} > 0$ are:

$$\tau_{bs}^{s^+} = \tau_{bs}^{sat}\left(1 - \exp\left(-\nu\gamma^{s^+}\right)\right), \tag{4}$$

$$\tau_{bs}^{s^-} = -A\tau_{bs}^{s^+}, \tag{5}$$

where τ_{bs}^{sat} is a saturation value of the backstress, A is a parameter allowing asymmetric evolution of the backstress magnitude on a slip system in two opposite directions s+ and s-, γ_b and ν are additional fitting parameters. The shear strain γ^s is taken from the point $\tau_{bs}^{s^+} = 0$. The laws for $d\gamma^{s^+} > 0$ and $\tau_{bs}^{s^+} < 0$ are:

$$\tau_{bs}^{s^+} = -(A+1)\tau_{bs}^{sat} \exp\left(-\frac{\gamma^{s^-}}{\gamma_b}\right) + \tau_{bs}^{sat} \tag{6}$$

$$\tau_{bs}^{s^-} = -\frac{1}{A}\tau_{bs}^{s^+} \tag{7}$$

where the shear strain γ^{s^-} is taken from the point of local reversal. The backstress influences the activation of slip systems as:

$$\boldsymbol{\sigma}^{c} \cdot \mathbf{m}^{s} - \tau_{bs}^{s} = \tau_{c}^{s}, \tag{8}$$

$$\widehat{\boldsymbol{\sigma}}^{c} \cdot \mathbf{m}^{s} - \dot{\tau}_{bs}^{s} = \dot{\tau}_{c}^{s}, \tag{9}$$

while the backstress evolves with shearing rates using:

$$\dot{\tau}_{bs}^{s} = \sum_{s'} h_{bs}^{ss'} \dot{\gamma}^{s'}, \tag{10}$$

where $h_{bs}^{ss'}$ is the backstress matrix. The law is as follows (Zecevic and Knezevic, 2019):

$$\boldsymbol{\tau_{bs}^{s}} = \mathbf{m}^{\boldsymbol{s}} \cdot \boldsymbol{\sigma_{bs}^{c}} = \boldsymbol{\tau_{bs,sys}^{s}} + \mathbf{2} \sum_{\boldsymbol{s'}} \mathbf{m}^{\boldsymbol{s}} \cdot \mathbf{m}^{\boldsymbol{s'}} \boldsymbol{\tau_{bs,sys*}^{s'}}, \tag{11}$$

where

$$\boldsymbol{\tau_{bs,sys*}^{s'}} = \begin{cases} \boldsymbol{\tau_{bs,sys}^{s'}} \boldsymbol{if}\ \boldsymbol{\tau_{bs,sys}^{s'}} > \mathbf{0} \\ \mathbf{0}\ \boldsymbol{if}\ \boldsymbol{\tau_{bs,sys}^{s'}} < \mathbf{0} \end{cases}. \tag{12}$$

In Eq. (11), σ_{bs}^{c} is the back-stress tensor based on the contribution from the slip system level sources over s' when $s' \neq s$. The slip system level back-stress is:

(if $d\gamma^{s^+} > 0$ and $\tau_{bs,sys}^{s^+} > 0$):

$$\boldsymbol{\tau_{bs,sys}^{s^+}} = \boldsymbol{\tau_{bs}^{sat}}\left(\mathbf{1} - \boldsymbol{exp}\left(-\boldsymbol{v\gamma^{s^+}}\right)\right), \tag{13}$$

$$\boldsymbol{\tau_{bs,sys}^{s^-}} = -\boldsymbol{A\tau_{bs,sys}^{s^+}}, \tag{14}$$

(if $d\gamma^{s^+} > 0$ and $\tau_{bs,sys}^{s^+} < 0$)

$$\boldsymbol{\tau_{bs,sys}^{s^+}} = -(\boldsymbol{A} + \mathbf{1})\boldsymbol{\tau_{bs}^{sat}}\, \boldsymbol{exp}\left(-\frac{\gamma^{s^-}}{\gamma_b}\right) + \boldsymbol{\tau_{bs}^{sat}}, \tag{15}$$

$$\boldsymbol{\tau_{bs,sys}^{s^-}} = -\frac{\mathbf{1}}{\boldsymbol{A}}\boldsymbol{\tau_{bs,sys}^{s^+}}. \tag{16}$$

The fitting parameters of the backstress law are a saturation value, τ_{bs}^{sat}, a parameter governing the asymmetric evolution, A, the denominator, γ_b, and a multiplier, v. The shearing strain, γ^{s}, is a value at the load reversal.

Model parameters for the hardening and backstress laws were calibrated through tensile tests and HREBSD scan data, performed in prior work (Sharma et al., 2022) on the AA 6016-T4 material. The same parameters, used in the present study, are shown in Tables 3-5 below.

Table 3. Latent hardening parameters.

a_0	a_1	a_2	a_3	a_4	a_5
0.068	0.068	0.0454	0.625	0.137	0.122

Table 4. Fitting parameters used for the evolution of slip resistance.

τ_0 [MPa]	k_1 $[m^{-1}]$	g	D [MPa]	$\rho_{for}^{s}[m^{-2}]$
25	1.38 x10^{8}	0.09	400	4.1e12

Table 5. Fitting parameters used for the evolution of slip system backstress.

τ_{bs}^{sat}[MPa]	ν	γ_b	A
18	560	0.001	1

In order to apply pre-strains to the sheet, appropriate boundary conditions were used in the model to reach the effective strain levels (i.e. 6%, 15%, 20%) that were achieved in the experiments for each desired pre-strain path, as seen in Figure 5.

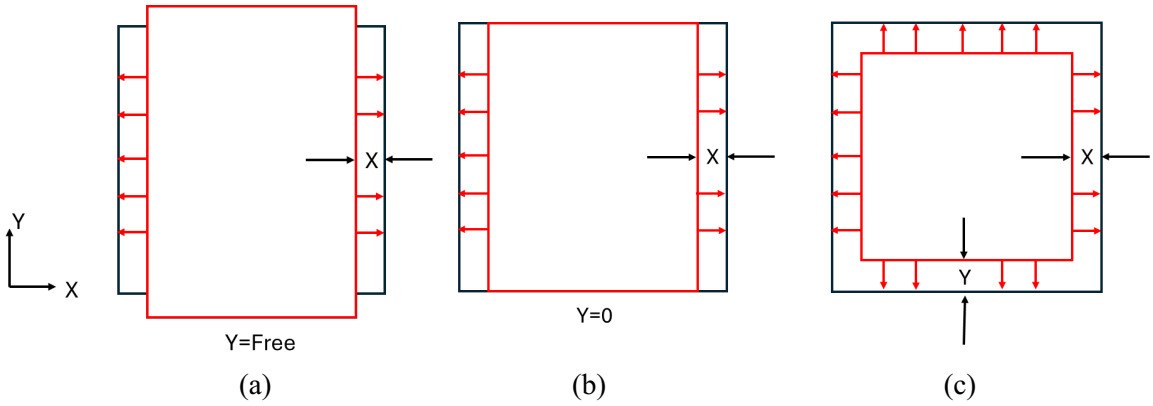

Fig. 5. Pre-strain simulations imparted various levels of effective strain to sheet blanks prior to the air bending/springback step. Boundary conditions are shown for pre-strain simulations in (a) uniaxial tension, (b) plane-strain tension, and (c) biaxial tension.

.

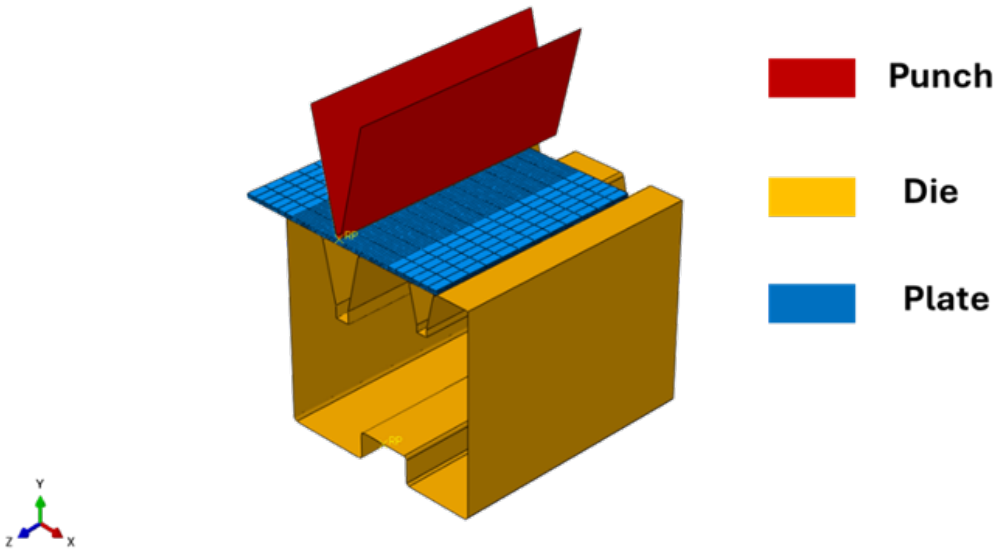

Fig. 6. Air bending model where the punch and die were both considered rigid for the purpose of the simulation. The punch/die bend angle was 30˚ and the punch radius was 0.8 mm. The sheet mesh, shown resting on the die, consisted of 1872 C3D20R elements, with 5 elements through the thickness.

The pre-strain simulation results were compared to experimentally measured pre-strains (using the DIC approach shown in Figure 2) for validation. Subsequently, after pre-strains were applied in the first simulation step, the bending/springback simulation was performed using the model tooling shown in Figure 6, where the sheet mesh had 1872 C3D20R elements, including 3 elements through the thickness, which was confirmed with a mesh sensitivity analysis. The tooling was considered rigid and isothermal for the purpose of these room temperature simulations

4 RESULTS AND DISCUSSION

Springback measurements for sheets pre-strained in uniaxial, plane-strain, and biaxial tension, to levels of 6%, 15%, and ~20% effective strain, are shown in Figure 7. For each bend angle, an increase in pre-strain led to a greater springback response. Specimens with biaxial tension pre-

strain exhibited the highest springback magnitude for most bend angles and pre-strain levels. One exception was the 20% biaxial pre-strain level and the 70° bend angle, where some minor cracking occurred on the outer surface of the sheet at the apex of the bend, indicating the limit of material ductility, and likely affecting the springback angle. Though the springback angles initially rise as the levels of pre-strain are increased, there is a saturation of this effect between 15% and 20%. This likely occurs as the yield stress stagnates at higher pre-strain levels. Figure 8 shows the evolution of dislocation density (DD) predicted by the CPFE-EPSC model for the pre-strain step, followed by the bending step (for a 15% effective pre-strain level) at the tensile tip of the sample. In this case, the model predicts the magnitude of statistically stored dislocations (SSD) but not geometrically necessary dislocation (GND). As seen in prior work, GND development typically occurs for lower levels of strain, associated with kinematic hardening (Sharma et al., 2022), while SSD development is associated with isotropic hardening at higher levels of strain.

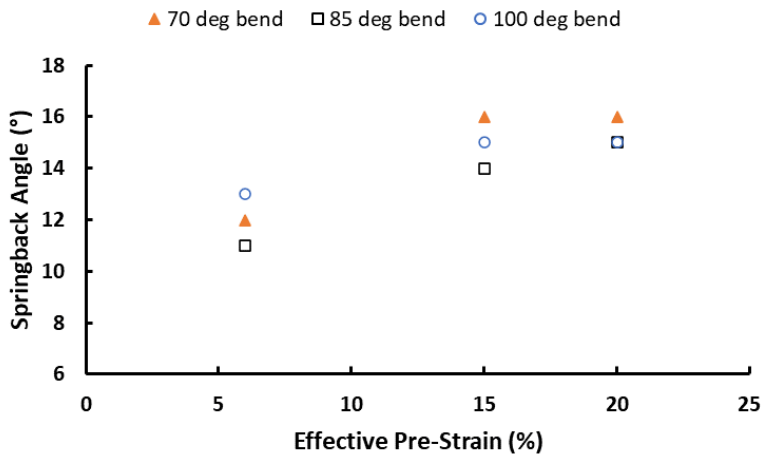

(a)

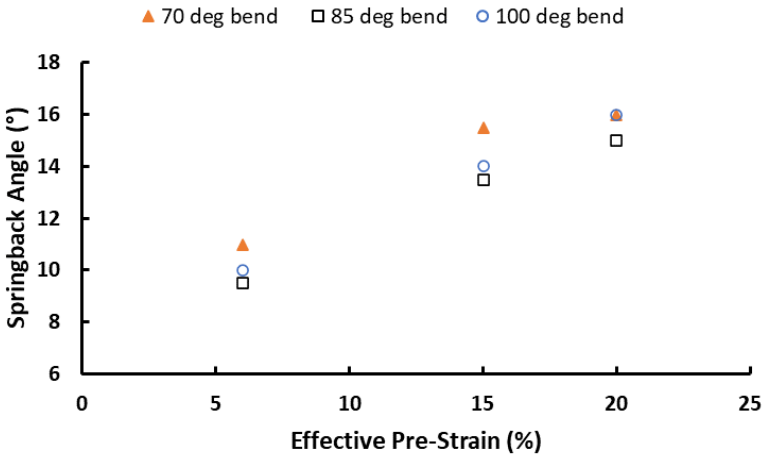

(b)

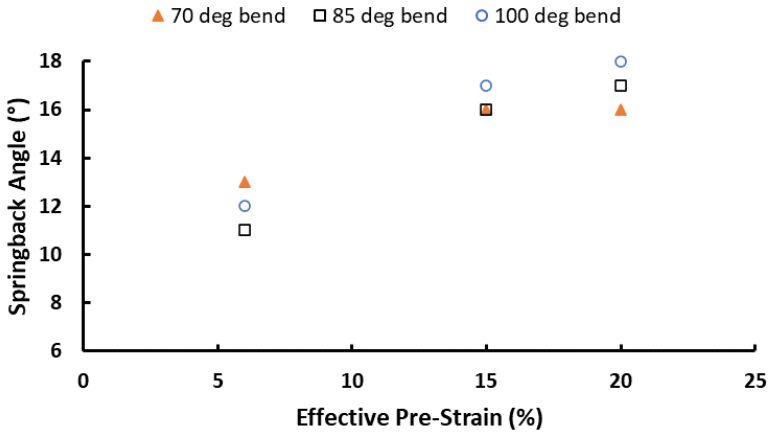

(c)

Figure 7. Springback angle as a function of pre-strain and bend magnitude for (a) uniaxial tension pre-strain, (b) plane-strain tension pre-strain, and (c) biaxial tension pre-strain. Each point represents an average of three replications.

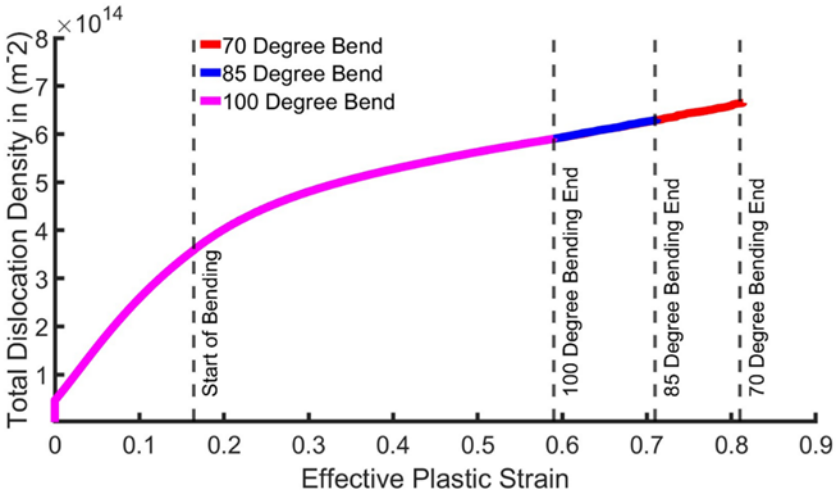

(a)

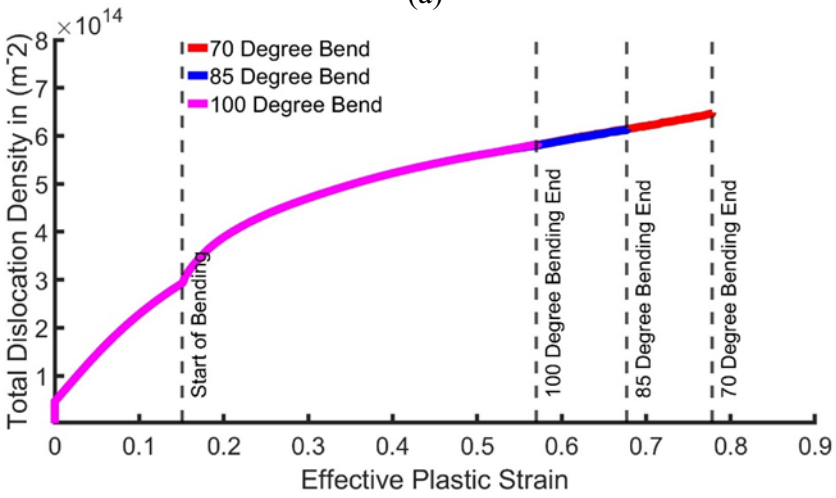

(b)

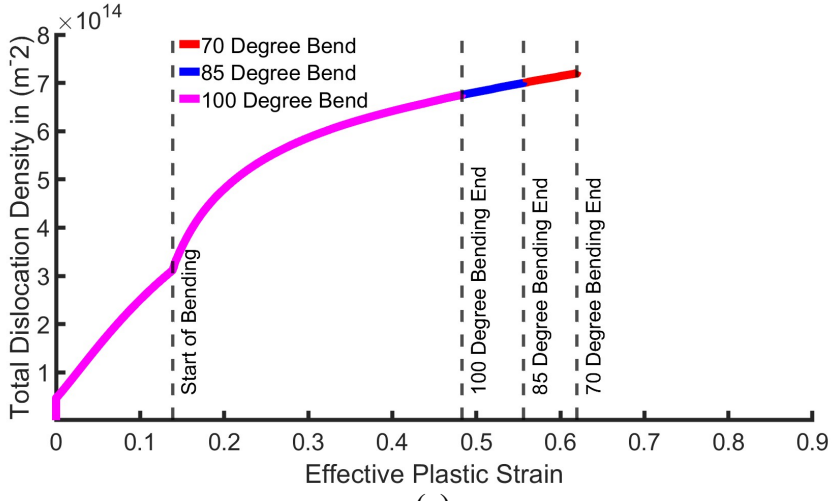

(c)

Figure 8. Rise in dislocation density predicted by CPFE – EPSC model at the apex of the bend as a function of effective plastic strain for (a) uniaxial pre-strain of 15% followed by bending, (b) plane-strain pre-strain of 15% followed by bending, and (c) biaxial tension pre-strain of 15% followed by bending. Note that initial SSD levels, after a 15% pre-strain, are different for each pre-strain path.

The transition from the end of pre-strain to the early stages of bending is relatively smooth for SSD development in the uniaxial and plane-strain pre-strain cases but is rather abrupt in the biaxial pre-strain case. Given that the bending step induces a plane-strain tension strain path on the outer portion of the sheet, for material on the tensile side of the neutral axis, a number of similar slip systems are re-activated during the bending step after first completing a plane-strain or uniaxial tension pre-strain step. The abrupt transition seen in the biaxial case is likely explained by activation of new slip systems during the initial stage of bending, promoting a sharper rise in predicted SSD content. While the model imparted the same equivalent strain to the specimens prior to bending (6%, 15%, 20%) the amount of SSD development generated during the pre-strain step was different for each strain path. Uniaxial pre-strain generated the highest level of SSD density; and the different levels of SSD for each type of pre-strain are likely related to texture of sheet. The r-value of aluminum is typically much lower than for steel, for example, so propensity for thinning of the sheet is greater; as such, biaxial tension, which promotes maximum thinning through the volume constancy principle, likely increased r-value through work hardening more than uniaxial tension. Biaxial tension also activates more slip systems than the other strain paths, thus more evenly distributing a given amount of plastic across them (Sharma et al., 2022).

Note that the effective plastic strain level achieved on the outer surface of the sheet, at its apex, was greatest for specimens with uniaxial pre-strain, followed by plane-strain tension, and finally biaxial tension. This could partly be accounted for by the thicknesses of each pre-strained sheet prior to bending. For a given level of pre-strain, the biaxial sheet would be thinnest, followed by plane-strain tension, then uniaxial tension. As such, a thinner sheet would generate lower plastic strains at the apex of the bend than a thicker one, for the same bend radius of the tool and air bending angle. For example, after an approximate 15% pre-strain, the model predicted the

following true thinning strains in the sheet blanks (depicted earlier in Figure 5): UT: -8.3%, PS: -13.2%, BT: -14.2%. The sheet thickness effect is part of the reason for the differences in effective strain at the end of each bend angle, but strain path is the other, as each one applies different levels of plastic strain along the eventual major strain direction that occurs during bending (perpendicular to the bend axis). As such, when the bending step does occur, the amount of additional major strain added to the pre-strain will be different. For example, a biaxial tension pre-strain only applies half of the effective strain along the eventual major strain direction that occurs during bending, ie ε_1 = 7.5% for a 15% effective strain target. When the bending step begins, additional major strain ε_1 is added to the surface of the sheet (point of interest in this case is at the apex of the bend) until the desired bend angle is reach (100˚, 85˚, or 70˚). For a uniaxial tension pre-strain, effective strain and ε_1 are the same, so for a 15% pre-strain ε_1 = 15% (and for 15% plane-strain tension pre-strain ε_1= 13.1%). Thus, as seen in Figure 8, the final effective strain after bending is greatest for the uniaxial tension pre-strain, followed closely by the plane-strain tension pre-strain, and finally the biaxial tension pre-strain. This analysis applies to the outer tensile surface of the sheet during bending and would not be as true for points closer to the neutral axis, or on the other side of the neutral axis, where the sheet material is in compression.

Figure 9 shows SSD development through the sheet thickness for the same types of pre-strain as shown in Figure 8, but only for a 70˚ bend, and a 15% pre-strain level. The SSD content was tracked at the four locations shown: on the inner surface (node 1), 0.33mm from the inner surface (node 2), 0.33mm from the outer surface (node 3), and on the outer surface (node 4). The inner surface (node 1) SSD development, in compression, is less than that of the outer surface (node 4), and the node 2 location appears to be the neutral surface for all three cases, where very little dislocation generation occurred after pre-strain.

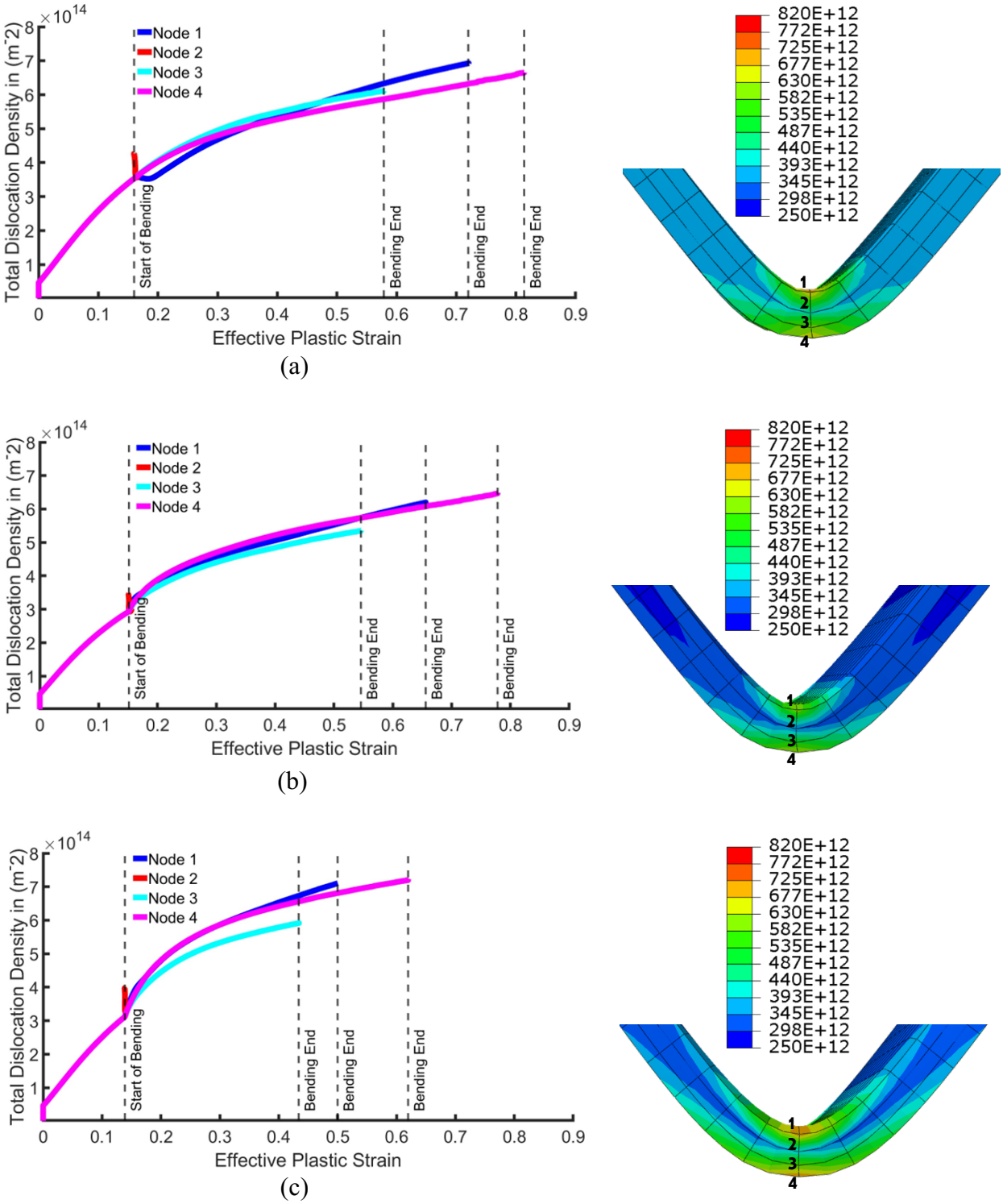

Figure 9. Rise in dislocation density predicted by CPFE – EPSC model at four locations through the thickness as a function of effective plastic strain for (a) uniaxial pre-strain of 15% followed by bending to 70˚, (b) plane-strain pre-strain of 15% followed by bending to 70˚, and (c) biaxial tension pre-strain of 15% followed by bending 70˚.

The small rise in SSD at node 2 during bending is done without an accompanying plastic strain increase and is an artifact to the averaging nature of SSD tracking at nodes, where neighboring integration points may contribute a small increase. Once again, it is interesting to note that while the biaxial tension pre-strain generated the smallest magnitude in SSD content at the end of 15% effective pre-strain, the SSD values for nodes 1, 3, and 4 terminate at the highest SSD content after bending to 70˚; uniaxial tension is second, while plane-strain tension is third. Also interesting is the drop in SSD at the start of bending, as the sheet goes into compression at node 1 for uniaxial tension pre-strain. The drop occurs owing to the reversible dislocations intrinsic to the strain path sensitive hardening law. As higher SSD content affects the backstress terms in the model, these observations are relevant to model accuracy, especially when backstress terms are not included in the simulation, as will be seen later.

The accuracy of the CPFE-EPSC model was assessed by comparing its predictions of springback angle with experiment, as seen in Figure 10. The maximum absolute error was about 2.5%, but most errors were less than 1%. This represents a very good level of accuracy across the different pre-strain conditions and levels, for the three different air bend angles. The model results shown in Figure 10 include the influence of backstress in the hardening law. As such, the high level of accuracy of the springback predictions confirms the need for a backstress component in the model, even when the effects of texture evolution are accounted for. The phenomenological form of the backstress model that was implemented (see eqns 13-16) is computationally efficient, thus providing motivation for adopting the current approach for industrial simulation of springback.

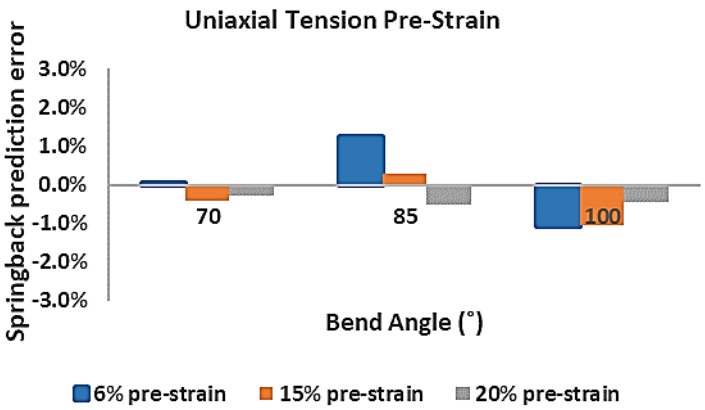

(a)

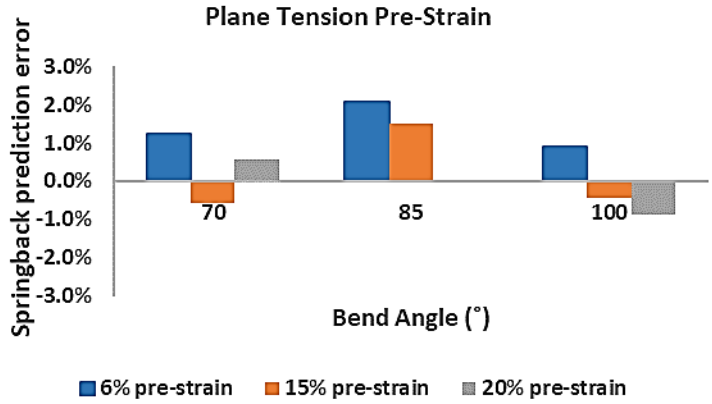

(b)

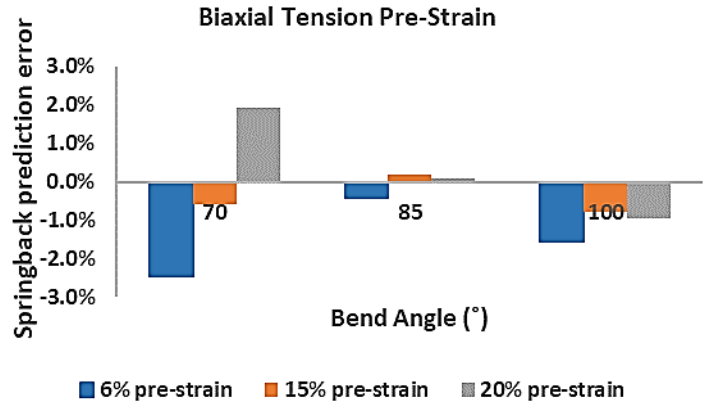

(c)

Figure 10. CPFE – EPSC model prediction error for pre-strain/bending/springback simulations for (a) uniaxial pre-strain of 15% followed by bending, (b) plane-strain pre-strain of 15% followed by bending, and (c) biaxial tension pre-strain of 15% followed by bending.

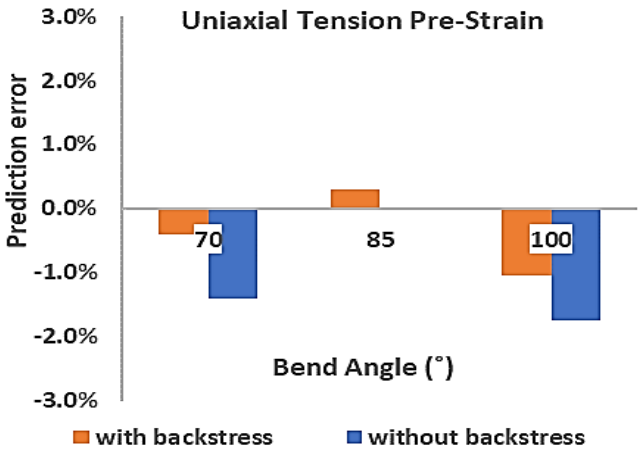

(a)

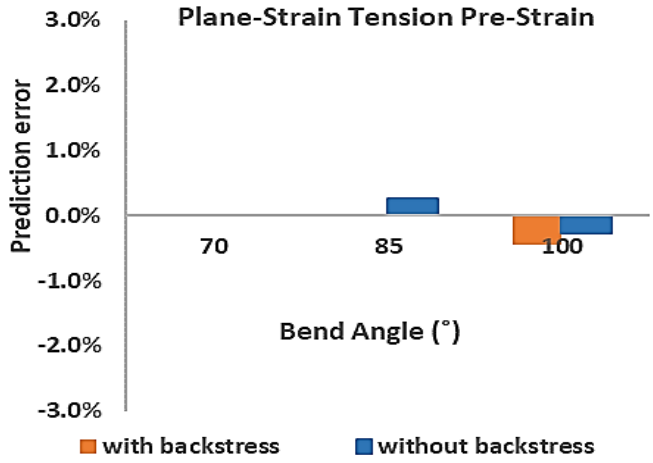

(b)

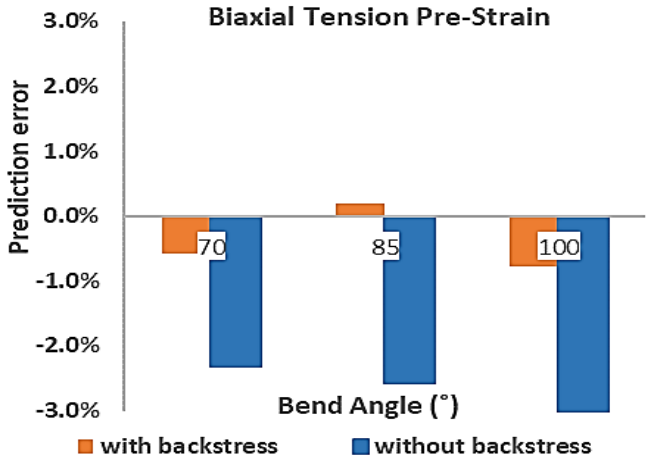

(c)

Figure 11. CPFE - EPSC model prediction error for pre-strain/bending/springback simulations where backstress was included in the hardening law (orange) and simulations where it was excluded (blue) for (a) uniaxial pre-strain of 15% followed by bending, (b) plane-strain pre-strain of 15% followed by bending, and (c) biaxial tension pre-strain of 15% followed by bending.

The influence of the backstress effect on accuracy of prediction was quantified by repeating model simulations without the backstress terms in the hardening law. In Figure 11, for the case of 15% pre-strain, the model results are compared for simulations with backstress, and without backstress. While the errors of the model without backstress are relatively small for the plane-strain pre-strain case, they are greater in the uniaxial pre-strain case, and much greater in the biaxial pre-strain case.

It is likely that the larger prediction errors for the biaxial pre-strain/bending/springback case seen in Figure 11 are a consequence of greater backstress development for this pre-strain path. For the plane strain pre-strain case, because bending also exhibits a plane-strain deformation mode, the same slip systems would be active during both steps, with plane-strain compression on one side of the neutral axis and plane strain tension on the other. By contrast, when the biaxial tension pre-strain step is followed by the bending step, there are some differences. Tables 3 and 4 show relative activities of slip systems from the model results, highlighted for both the pre-strain (at 80% of pre-strain target) and bending (at 60% of bending target) steps, and taken at the apex of the bend on both the tensile surface and the compression surface. Evidently, for the plane-strain/bending case the same slip systems are active across both steps, while slip activity amounts slightly shift during the bending step relative to the pre-strain step for both the compression and tensile surfaces of the sheet, but with a larger shift on the compression side. For the biaxial tension/bending case, the (-1 -1 1)<1 0 1> slip system that is active during pre-strain becomes less during bending, while the (1 -1 1)<-1 0 1> slip system that is less active during pre-strain becomes active during bending revealing greater shifts in the relative activities from the biaxial tension to bending than froms the plane-strain to bending. In total, 5 slip systems were active during the biaxial tension pre-strain/bending steps, in contrast to 5 for the compression surface and 4 on the tensile surface of the sheet for the plane-strain tension pre-strain/ bending case.

Table 3. Plane-Strain Tension Pre-Strain Followed by Bending

Compression Surface at Bend Apex

Slip Plane			Slip Direction			Pre-Strain	Bending
n			b			Slip Activity	Slip Activity
-1	1	1	0	-1	1	0.1217	0.2158
-1	1	1	1	0	1	0.2069	0.1648
-1	1	1	1	1	0	0.0935	0.1110
1	1	1	0	-1	1	0.0838	0.0903
1	1	1	-1	0	1	0.0322	0.0147
1	1	1	-1	1	0	0.0149	0.0216
-1	-1	1	0	1	1	0.0472	0.0249
-1	-1	1	1	0	1	0.0213	0.0356
-1	-1	1	-1	1	0	0.0414	0.0289
1	-1	1	0	1	1	0.0271	0.0374
1	-1	1	-1	0	1	0.1598	0.1290
1	-1	1	1	1	0	0.1502	0.1260

Tensile Surface at Bend Apex

Slip Plane			Slip Direction			Pre-Strain	Bending
n			b			Slip Activity	Slip Activity
-1	1	1	0	-1	1	0.1217	0.1129
-1	1	1	1	0	1	0.2068	0.2039
-1	1	1	1	1	0	0.0934	0.0763
1	1	1	0	-1	1	0.0838	0.0767
1	1	1	-1	0	1	0.0322	0.0228
1	1	1	-1	1	0	0.0149	0.0200
-1	-1	1	0	1	1	0.0472	0.0529
-1	-1	1	1	0	1	0.0213	0.0197
-1	-1	1	-1	1	0	0.0414	0.0565

Compression Surface at Bend Apex

Slip Plane			Slip Direction			Pre-Strain	Bending
n			b			Slip Activity	Slip Activity
-1	1	1	0	-1	1	0.1113	0.2152
-1	1	1	1	0	1	0.1737	0.1473
-1	1	1	1	1	0	0.1526	0.1063
1	1	1	0	-1	1	0.0410	0.0857
1	1	1	-1	0	1	0.0733	0.0178
1	1	1	-1	1	0	0.0166	0.0340
-1	-1	1	0	1	1	0.0037	0.0283
-1	-1	1	1	0	1	0.1168	0.0457
-1	-1	1	-1	1	0	0.0039	0.0331
1	-1	1	0	1	1	0.0978	0.0503
1	-1	1	-1	0	1	0.0964	0.1196
1	-1	1	1	1	0	0.1129	0.1169
1	-1	1	0	1	1	0.0271	0.0236
1	-1	1	-1	0	1	0.1599	0.1717
1	-1	1	1	1	0	0.1502	0.1631

Table 4. Biaxial Tension Pre-Strain Followed by Bending

Tensile Surface at Bend Apex

Slip Plane			Slip Direction			Pre-Strain	Bending
n			b			Slip Activity	Slip Activity
-1	1	1	0	-1	1	0.1112	0.1270
-1	1	1	1	0	1	0.1737	0.2148
-1	1	1	1	1	0	0.1526	0.0860
1	1	1	0	-1	1	0.0409	0.0720
1	1	1	-1	0	1	0.0732	0.0320
1	1	1	-1	1	0	0.0166	0.0135
-1	-1	1	0	1	1	0.0037	0.0538
-1	-1	1	1	0	1	0.1167	0.0172
-1	-1	1	-1	1	0	0.0040	0.0524
1	-1	1	0	1	1	0.0978	0.0234
1	-1	1	-1	0	1	0.0965	0.1563
1	-1	1	1	1	0	0.1129	0.1516

When considering both the compression and tensile surfaces, the biaixal tension pre-strain case has a total of twelve active slip systems (6 on each surface), versus a total of 9 for the plane-strain tension pre-strain case. Thus backstress development, which is proportional to slip activity on a given system, is greater in the first case and is the reason for poor predictdion accuracy seen in Fig. 11c when backstress was not included in the model.

The case of the 100˚ bend after 15% biaxial pre-strain, which exhibited the greatest prediction error when backstress was not included in the simulation, is shown in Figure 12. Without backstress the predicted included angle after springback, on right, was 113.3˚, versus actual measurement of 117˚. This level of error is not acceptable for most practical parts assembly applications, as the prediction would lead to a design where mating part surfaces would not be in contact for joining , for example.

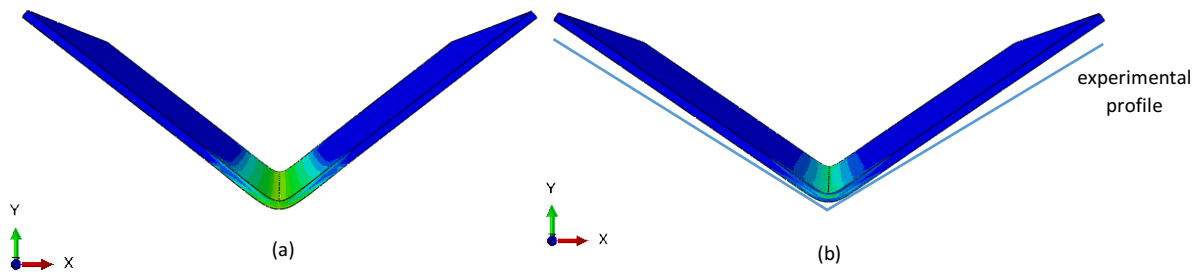

Figure 12. von Mises stresses at the end of the bending step, for the 15% biaxial pre-strain case: (a) end of bending, and (b) after springback.

5 SUMMARY AND CONCLUSIONS

Air bending experiments were performed on AA 6016-T4 sheet material, where pre-strains were first applied to the sheet specimens in uniaxial tension, plane-strain tension, and biaxial tension, at effective strain levels of 6%, 15% and ~20%. The pre-strained specimens were then subjected to bending in a v-die, using target angles of 100˚, 85˚, and 70˚, after which springback was measured. It was found that greater levels of pre-strain resulted in larger springback magnitudes, and that the biaxially pre-strained specimens generally exhibited greater springback levels than the other pre-strained specimens. A CPFE – EPSC model with phenomenological backstress component in the strain path sensitive hardening law was used to predict springback magnitude across the different pre-strain paths, levels, and imposed air bend angles. It was observed that the more significant the strain path change, the greater the influence of backstress on model accuracy, owing to the activation of new slip systems after the change. This was correlated to greater SSD development on both the tensile surface of the sheet, and also through the thickness. When the strain path change was less abrupt, as was seen in the case of plane-strain pre-strain followed by bending, SSD development was not as great and the effect of backstress on model accuracy was less significant, with the same slip systems active during both pre-strain and bending. The use of a phenomenological backstress law, within the CPFE-EPSC framework, is seen to be an accurate and efficient approach to modeling springback prediction in Al alloys, especially when strain path changes occur during forming, as is common for industrial applications.

ACKNOWLEDGEMENTS

The work presented in this paper was supported by the National Science Foundation grant numbers CMMI-1926662 (BYU) and CMMI-1926677 (UNH). The AA 6016-T4 sheet material used for experiments was provided by Commonwealth Aluminum (Madison Heights, MI).

APPENDIX A

This appendix summarizes the CPFE-EPSC details, including the EPSC material model and strain path sensitive hardening law for the evolution of slip resistance.

A.1 EPSC material model

A crystal plasticity model based on the EPSC formulation was used to perform the simulations in the present work. The model is an implicit EPSC model coupled with the implicit FEM framework, termed CPFE-EPSC (Zecevic and Knezevic, 2019). The description uses $\cdot$ and $\otimes$ to denote scalar/dot and oughter/tensor products, respectively. The polycrystalline aggregate of AA 6016 in EPSC is represented by a set of weighted grains/inclusions. Every grain/inclusion is an elasto-plastic continuum interacting with a HEM (homogeneous equivalent matrix). Every inclusion has a distinct crystallography/orientation, volume fraction, and ellipsoidal shape. The former two evolve with plastic strain.

The EPSC model implements the following constitutive equation:

$$\widehat{\boldsymbol{\sigma}} = \dot{\boldsymbol{\sigma}} + \boldsymbol{\sigma}\mathbf{W} - \mathbf{W}\boldsymbol{\sigma}, \tag{A1}$$

for calculating the Jaumann, $\widehat{\boldsymbol{\sigma}}$ (Nagtegaal and Veldpaus, 1984; Neil et al., 2010). The equation applies to a material point, which can be a single crystal or an aggregate. The other tensors in the equation, $\mathbf{W}$ and $\boldsymbol{\sigma}$ are the spin and Cauchy stress tensors, respectively. The corresponding tensors at the crystal level are denoted with a superscript *c*, so $\mathbf{W}^c$ and $\boldsymbol{\sigma}^c$. The Jaumann rate at the crystal level is $\widehat{\boldsymbol{\sigma}}^c$ is

$$\widehat{\boldsymbol{\sigma}}^c = \mathbf{C}^c(\dot{\boldsymbol{\varepsilon}}^c - \dot{\boldsymbol{\varepsilon}}^{pl,c}) - \boldsymbol{\sigma}^c tr(\dot{\boldsymbol{\varepsilon}}^c), \tag{A2}$$

where $\mathbf{C}^c$ is the 4th rank tensor of crystal level elastic stiffness, $\dot{\boldsymbol{\varepsilon}}^c$ is the strain rate at the crystal level, and $\dot{\boldsymbol{\varepsilon}}^{pl,c}$ is the plastic part of the strain rate. The plastic portion of the strain rate is obtained as a sum of the products between the symmetric Schmid matrix, $\mathbf{m}^s = \frac{1}{2}(\mathbf{b}^s \otimes \mathbf{n}^s + \mathbf{n}^s \otimes \mathbf{b}^s)$ and shearing rates, $\dot{\gamma}^s$, over active slip systems, s, per grain, *c,* i.e. $\dot{\boldsymbol{\varepsilon}}^{pl,c} = \mathbf{m}^s\dot{\gamma}^s$. The Schmid tensors represents the geometry of the slip directions parallel to the Burgers vector, $\mathbf{b}^s$, and the plane normal, $\mathbf{n}^s$.

The crystal level and polycrystal level stress and strain rate relations can also be expressed as

$$\widehat{\boldsymbol{\sigma}}^c = \mathbf{L}^c(\dot{\boldsymbol{\varepsilon}}^c - \dot{\boldsymbol{\varepsilon}}^{pt,c}), \tag{A3a}$$

$$\widehat{\boldsymbol{\sigma}} = \mathbf{L}(\dot{\boldsymbol{\varepsilon}} - \dot{\boldsymbol{\varepsilon}}^{pt}), \tag{A3b}$$

where $\mathbf{L}^c$ and $\mathbf{L}$ are the elasto-plastic stiffness tensors at the crystal and polycrystal levels. The former is derived from Eq. (A2) and using the hardening law, while the latter is obtained using the self-consistent (SC) homogenization procedure (Eshelby, 1957; Lipinski and Berveiller, 1989; Neil et al., 2010; Turner and Tomé, 1994; Zecevic et al., 2015). The procedure begins from the volume averages of stress and strain-rate, $\dot{\boldsymbol{\varepsilon}}$

$$\widehat{\boldsymbol{\sigma}} = \langle \widehat{\boldsymbol{\sigma}}^c \rangle \text{ and } \dot{\boldsymbol{\varepsilon}} = \langle \dot{\boldsymbol{\varepsilon}}^c \rangle. \tag{A4}$$

Activation of slip systems is based on the two conditions:

$$\boldsymbol{\sigma}^c \cdot \mathbf{m}^s = \tau_c^s, \tag{A5a}$$

$$\widehat{\boldsymbol{\sigma}}^c \cdot \mathbf{m}^s = \dot{\tau}_c^s, \tag{A5b}$$

where, τ_c^s is the current slip resistance, which will be defined in A.2. The first condition ensures that the stress glides on the yield surface of crystals, while the second condition is the consistency condition ensuring that the stress persists on the surface of crystals (Knockaert et al., 2000; Zecevic et al., 2019).

Crystal lattice evolution is accounted for using the spin tensors:

$$\mathbf{W}^c = \mathbf{W}^{c,app} - \mathbf{W}^{pl,c}, \tag{A6}$$

where $\mathbf{W}^{c,app}$ and $\mathbf{W}^{pl,c}$ are applied and plastic rotation rate/spin tensors. The latter is $\mathbf{W}^{pl,c} = \sum_s \dot{\gamma}^s \mathbf{q}^s$ with $\mathbf{q}^s = \frac{1}{2}(\mathbf{b}^s \otimes \mathbf{n}^s - \mathbf{n}^s \otimes \mathbf{b}^s)$.

A.2 Hardening law

s+ and *s-* indicate positive and negative directions of slip systems in the description that follows, while both positive and negative directions are included in *s*. α enumerates slip modes/families, which for AA6016-T4 is only octahedral slip family $\alpha = 1$, $\{111\}\langle 1\bar{1}0\rangle$. The hardening law available in the present model is formulated based on the evolution of statistical dislocation densities (Beyerlein and Tomé, 2008; Knezevic et al., 2014). The law has been used in capturing the mechanical response and texture evolution of AA6016-T4 (Daroju et al., 2022) and AA6022-T4 (Zecevic and Knezevic, 2015; Zecevic and Knezevic, 2018).
The slip resistance is:

$$\tau_c^s = \tau_0^\alpha + \tau_{forest}^s + \tau_{debris}^\alpha, \tag{A7}$$

where τ_0^α is an initial slip resistance that does not evolve, τ_{forest}^s is a contribution from statistically stored dislocations that evolve, and τ_{debris}^α is a contribution from dislocations stored as debris that also evolve. The forest term is:

$$\tau_{forest}^s = b^\alpha \chi \mu^\alpha \sqrt{\textstyle\sum_{s'} L^{ss'} \rho_{tot}^{s'}} \tag{A8}$$

where $b^{\alpha} = 2.86\ 10^{-10}$ m is the Burgers vector for AA, $\chi = 0.9$ is a strength of dislocation/dislocation interaction constant, ρ_{tot}^{s} is the total dislocation density of forests for s^{th} slip system, and $L^{ss\prime}$ is a latent interaction matrix based on (Franciosi and Zaoui, 1982; Khadyko et al., 2016). Entries of the latent matrix are based on simulations presented in (Devincre et al., 2006; Hoc et al., 2004).

The debris/substructure contributing term is:

$$\tau_{debris}^{\alpha} = 0.086\mu^{\alpha}b^{\alpha}\sqrt{\rho_{deb}}log\left(\frac{1}{b^{\alpha}\sqrt{\rho_{deb}}}\right) \tag{A9}$$

where ρ_{deb} is the dislocation density of debris/substructure type (Madec et al., 2003).
The total dislocation density is:

$$\rho_{tot}^{s} = \rho_{for}^{s} + \rho_{rev}^{s^{+}} + \rho_{rev}^{s^{-}}, \tag{A10}$$

where ρ_{for}^{s} is the forward on s, while $\rho_{rev}^{s^{+}}$ and $\rho_{rev}^{s^{-}}$ are the reversible dislocation densities on the s^{+} and s^{-} providing strain path sensitivity in combination with backstress. The evolution of these dislocation densities with shearing strains is (Khadyko et al., 2016; Kitayama et al., 2013; Kocks and Mecking, 1981)

(If $d\gamma^{s^{+}} > 0$)

$$\frac{\partial \rho_{for}^{s}}{\partial \gamma^{s}} = (1-p)k_1^{\alpha}\sqrt{\sum_{s\prime} g^{ss\prime}\rho_{tot}^{s\prime}} - k_2^{\alpha}(\dot{\varepsilon},T)\rho_{for}^{s}, \tag{A11a}$$

$$\frac{\partial \rho_{rev}^{s^{+}}}{\partial \gamma^{s}} = pk_1^{\alpha}\sqrt{\sum_{s\prime} g^{ss\prime}\rho_{tot}^{s\prime}} - k_2^{\alpha}(\dot{\varepsilon},T)\rho_{rev}^{s^{+}}, \tag{A12a}$$

$$\frac{\partial \rho_{rev}^{s^{-}}}{\partial \gamma^{s}} = -k_1^{\alpha}\sqrt{\sum_{s\prime} g^{ss\prime}\rho_{tot}^{s\prime}}\left(\frac{\rho_{rev}^{s^{-}}}{\rho_0^{s}}\right)^{m}, \tag{A13a}$$

(If $d\gamma^{s^{-}} > 0$)

$$\frac{\partial \rho_{for}^{s}}{\partial \gamma^{s}} = (1-p)k_1^{\alpha}\sqrt{\sum_{s\prime} g^{ss\prime}\rho_{tot}^{s\prime}} - k_2^{\alpha}(\dot{\varepsilon},T)\rho_{for}^{s}, \tag{A11b}$$

$$\frac{\partial \rho_{rev}^{s^{+}}}{\partial \gamma^{s}} = -k_1^{\alpha}\sqrt{\sum_{s\prime} g^{ss\prime}\rho_{tot}^{s\prime}}\left(\frac{\rho_{rev}^{s^{+}}}{\rho_0^{s}}\right)^{m}, \tag{A12b}$$

$$\frac{\partial \rho_{rev}^{s^{-}}}{\partial \gamma^{s}} = pk_1^{\alpha}\sqrt{\sum_{s\prime} g^{ss\prime}\rho_{tot}^{s\prime}} - k_2^{\alpha}(\dot{\varepsilon},T)\rho_{rev}^{s^{-}}, \tag{A13b}$$

The initial conditions are:

$$\rho_{for}^{s}(\gamma^{s}=0) = 4.1\times 10^{12}\ m^{-2},\ \rho_{rev}^{s^{+}}(\gamma^{s}=0) = 0 \text{ and } \rho_{rev}^{s^{-}}(\gamma^{s}=0) = 0. \tag{A14}$$

In the above equations, k_1^{α} is one of the fitting parameters controlling the rate of generation of dislocations, k_2^{α} is a temperature (T) and strain rate ($\dot{\varepsilon}$) sensitive parameter driving dynamic recovery, p is a reversibility parameter taken as 0.2, $g^{ss\prime}$ is another interaction matrix set to $g^{ss} = 1$ and $g^{ss\prime} = 1$ (Khadyko et al., 2016; Kocks et al., 1991; Teodosiu and Raphanel, 1991),

m is a constant governing the rate of dislocation recombination set to 0.5 (Wen et al., 2015), and ρ_0^s is the total dislocation density at the point of reversal (Kitayama et al., 2013).

The coefficient k_2^α is:

$$\frac{k_2^\alpha}{k_1^\alpha} = \frac{\chi b^\alpha}{g^\alpha}\left(1 - \frac{k_B T}{D^\alpha (b^\alpha)^3} ln\left(\frac{\dot{\varepsilon}}{\dot{\varepsilon}_0}\right)\right), \tag{A15}$$

where, k_B is the Boltzmann constant, $\dot{\varepsilon}_0 = 10^7$ is a reference strain-rate, g^α is another fitting parameter representing effective activation enthalpy, and D^α is yet another fitting parameter representing drag stress. The debris/substructure dislocation density evolves using:

$$\frac{\partial \rho_{deb}}{\partial \gamma^s} = q^\alpha b^\alpha \sqrt{\rho_{deb}}\, k_2^\alpha(\dot{\varepsilon}, T)\rho_{tot}^s, \tag{A16}$$

where q^α is a last fitting parameter determining the number of dislocations that become debris/substructure. The debris dislocation density evolves from a very small value of 0.1 m^{-2}.

A.3 FE-EPSC model

SC models have been coupled with the implicit FEM as UMATs in earlier works (Knezevic et al., 2013; Marki et al., 2022; Zecevic et al., 2017; Zecevic and Knezevic, 2017, 2019). The code from (Zecevic and Knezevic, 2019) is used in the present work.

DATA AVAILABILITY

The raw/processed data required to reproduce these findings will be made available upon request.

REFERENCES

Ashby, M.F., 1970. The deformation of plastically non-homogeneous materials. Phil. Mag. 21, 399-424.

Barrett, T.J., Eghtesad, A., McCabe, R.J., Clausen, B., Brown, D.W., Vogel, S.C., Knezevic, M., 2019. A generalized spherical harmonics-based procedure for the interpolation of partial datasets of orientation distributions to enable crystal mechanics-based simulations. Materialia 6, 100328.

Barrett, T.J., Knezevic, M., 2019. Deep drawing simulations using the finite element method embedding a multi-level crystal plasticity constitutive law: Experimental verification and sensitivity analysis. Computer Methods in Applied Mechanics and Engineering 354, 245-270.

Beyerlein, I.J., Tomé, C.N., 2008. A dislocation-based constitutive law for pure Zr including temperature effects. International Journal of Plasticity 24, 867-895.

Boers, S.H.A., Schreurs, P.J.G., Geers, M.G.D., Levkovitch, V., Wang, J., Svendsen, B., 2010. Experimental characterization and model identification of directional hardening effects in metals for complex strain path changes. International Journal of Solids and Structures 47, 1361-1374.

Chen, S., Liao, J., Xiang, H., Xue, X., Pereira, A.B., 2021. Pre-strain effect on twist springback of a 3D P-channel in deep drawing. Journal of Materials Processing Technology 287, 116224.

Cheng, J., Green, D.E., Golovashchenko, S.F., 2017. Formability enhancement of DP600 steel sheets in electro-hydraulic die forming. Journal of Materials Processing Technology 244, 178-189.

Chongthairungruang, B., Uthaisangsuk, V., Suranuntchai, S., Jirathearanat, S., 2012. Experimental and numerical investigation of springback effect for advanced high strength dual phase steel. Materials & Design 39, 318-328.

Daroju, S., Kuwabara, T., Sharma, R., Fullwood, D.T., Miles, M.P., Knezevic, M., 2022. Experimental characterization and crystal plasticity modeling for predicting load reversals in AA6016-T4 and AA7021-T79. International Journal of Plasticity 153, 103292.

Devincre, B., Kubin, L., Hoc, T., 2006. Physical analyses of crystal plasticity by DD simulations. Scripta Materialia 54, 741-746.

Eghtesad, A., Barrett, T.J., Knezevic, M., 2018. Compact reconstruction of orientation distributions using generalized spherical harmonics to advance large-scale crystal plasticity modeling: Verification using cubic, hexagonal, and orthorhombic polycrystals. Acta Materialia 155, 418-432.

El-Madhoun, Y., Mohamed, A., Bassim, M., 2003. Cyclic stress–strain response and dislocation structures in polycrystalline aluminum. Materials Science and Engineering: A 359, 220-227.

Eshelby, J.D., 1957. The determination of the elastic field of an ellipsoidal inclusion, and related problems. Proc R. Soc. Lond. A 241, 376-396.

Field, D.P., Trivedi, P.B., Wright, S.I., Kumar, M., 2005. Analysis of local orientation gradients in deformed single crystals. Ultramicroscopy 103, 33-39.

Franciosi, P., Zaoui, A., 1982. Multislip in f.c.c. crystals a theoretical approach compared with experimental data. Acta Metallurgica 30, 1627-1637.

Hoc, T., Devincre, B., Kubin, L., 2004. Deformation stage I of FCC crystals: Constitutive modelling, 25 th Riso International Symposium on Materials Science 2004, pp. 43-59.

Joo, M., Wi, M.S., Yoon, S.Y., Lee, S.Y., Barlat, F., Tomé, C.N., Jeon, B., Jeong, Y., 2023. A crystal plasticity finite element analysis on the effect of prestrain on springback. Int J Mech Sci 237.

Khadyko, M., Dumoulin, S., Cailletaud, G., Hopperstad, O.S., 2016. Latent hardening and plastic anisotropy evolution in AA6060 aluminium alloy. International Journal of Plasticity 76, 51-74.
Kitayama, K., Tomé, C.N., Rauch, E.F., Gracio, J.J., Barlat, F., 2013. A crystallographic dislocation model for describing hardening of polycrystals during strain path changes. Application to low carbon steels. International Journal of Plasticity 46, 54-69.
Knezevic, M., Beyerlein, I.J., Lovato, M.L., Tomé, C.N., Richards, A.W., McCabe, R.J., 2014. A strain-rate and temperature dependent constitutive model for BCC metals incorporating non-Schmid effects: Application to tantalum–tungsten alloys. International Journal of Plasticity 62, 93-104.
Knezevic, M., Landry, N.W., 2015. Procedures for reducing large datasets of crystal orientations using generalized spherical harmonics. Mechanics of Materials 88, 73-86.
Knezevic, M., McCabe, R.J., Lebensohn, R.A., Tomé, C.N., Liu, C., Lovato, M.L., Mihaila, B., 2013. Integration of self-consistent polycrystal plasticity with dislocation density based hardening laws within an implicit finite element framework: Application to low-symmetry metals. Journal of the Mechanics and Physics of Solids 61, 2034-2046.
Knockaert, R., Chastel, Y., Massoni, E., 2000. Rate-independent crystalline and polycrystalline plasticity, application to FCC materials. International Journal of Plasticity 16, 179-198.
Kocks, U.F., Franciosi, P., Kawai, M., 1991. A Forest Model of Latent Hardening and its Application to Polycrystal Deformations. Textures and Microstructures 14, 1103-1114.
Kocks, U.F., Mecking, H., 1981. Kinetics of Flow and Strain-Hardening. Acta Metallurgica 29, 1865-1875.
Liao, J., Chen, S., Xue, X., Xiang, H., 2020. On twist springback of a curved channel with pre-strain effect. International Journal of Lightweight Materials and Manufacture 3, 108-112.
Lipinski, P., Berveiller, M., 1989. Elastoplasticity of micro-inhomogeneous metals at large strains. International Journal of Plasticity 5, 149-172.
Madec, R., Devincre, B., Kubin, L., Hoc, T., Rodney, D., 2003. The role of collinear interaction in dislocation-induced hardening. Science 301, 1879-1882.
Marki, R.E., Brindley, K.A., McCabe, R.J., Knezevic, M., 2022. Crystal mechanics-based thermo-elastic constitutive modeling of orthorhombic uranium using generalized spherical harmonics and first-order bounding theories. Journal of Nuclear Materials 560, 153472.
Nagtegaal, J.C., Veldpaus, F.E., 1984. On the implementation of finite strain plasticity equations in a numerical model. Numerical methods in industrial forming processes, 351-371.
Neil, C.J., Wollmershauser, J.A., Clausen, B., Tomé, C.N., Agnew, S.R., 2010. Modeling lattice strain evolution at finite strains and experimental verification for copper and stainless steel using in situ neutron diffraction. International Journal of Plasticity 26, 1772-1791.
Sharma, R., Sargeant, D., Daroju, S., Kenezevic, M., Miles, M.P., Fullwood, D.T., 2022. Multi-strain path deformation behavior of AA6016-T4: Experiments and crystal plasticity modeling. International Journal of Solids and Structures, 111536.
Shen, Z., Wagoner, R.H., Clark, W.A.T., 1988. Dislocation and grain boundary interactions in metals. Acta Metall. 36, 3231-3242.
Teodosiu, C., Raphanel, J.L., 1991. Finite element simulations of large elastoplastic deformations of multicrystals. Proceedings of the International Seminar MECAMAT91, 153-168.
Turner, P.A., Tomé, C.N., 1994. A study of residual stresses in Zircaloy-2 with rod texture. Acta Metallurgica et Materialia 42, 4143-4153.

Uemori, T., Sumikawa, S., Naka, T., Ma, N.S., Yoshida, F., 2017. Influence of Bauschinger Effect and Anisotropy on Springback of Aluminum Alloy Sheets. Mater Trans 58, 921-926.
Wagoner, R.H., Lim, H., Lee, M.-G., 2013. Advanced Issues in springback. International Journal of Plasticity 45, 3-20.
Wen, W., Borodachenkova, M., Tomé, C.N., Vincze, G., Rauch, E.F., Barlat, F., Grácio, J.J., 2015. Mechanical behavior of Mg subjected to strain path changes: Experiments and modeling. International Journal of Plasticity 73, 171-183.
Yue, Z., Qi, J., Zhao, X., Badreddine, H., Gao, J., Chu, X., 2018. Springback Prediction of Aluminum Alloy Sheet under Changing Loading Paths with Consideration of the Influence of Kinematic Hardening and Ductile Damage. Metals 2018, Vol. 8, Page 950 8, 950-950.
Zecevic, M., Beyerlein, I.J., Knezevic, M., 2017. Coupling elasto-plastic self-consistent crystal plasticity and implicit finite elements: Applications to compression, cyclic tension-compression, and bending to large strains. International Journal of Plasticity 93, 187-211.
Zecevic, M., Knezevic, M., 2015. A dislocation density based elasto-plastic self-consistent model for the prediction of cyclic deformation: Application to Al6022-T4. International Journal of Plasticity 72, 200-217.
Zecevic, M., Knezevic, M., 2017. Modeling of Sheet Metal Forming Based on Implicit Embedding of the Elasto-Plastic Self-Consistent Formulation in Shell Elements: Application to Cup Drawing of AA6022-T4. JOM 69, 922-929.
Zecevic, M., Knezevic, M., 2018. Latent hardening within the elasto-plastic self-consistent polycrystal homogenization to enable the prediction of anisotropy of AA6022-T4 sheets. International Journal of Plasticity 105, 141-163.
Zecevic, M., Knezevic, M., 2019. An implicit formulation of the elasto-plastic self-consistent polycrystal plasticity model and its implementation in implicit finite elements. Mechanics of Materials 136, 103065.
Zecevic, M., Knezevic, M., Beyerlein, I.J., Tomé, C.N., 2015. An elasto-plastic self-consistent model with hardening based on dislocation density, twinning and de-twinning: Application to strain path changes in HCP metals. Materials Science and Engineering: A 638, 262-274.
Zecevic, M., Upadhyay, M.V., Polatidis, E., Panzner, T., Van Swygenhoven, H., Knezevic, M., 2019. A crystallographic extension to the Olson-Cohen model for predicting strain path dependence of martensitic transformation. Acta Materialia 166, 386-401.